Segmental Orientations and Deformation Mechanism of Poly(ether-*block*-amide) Films†

Yihu Song,‡ Hiroko Yamamoto,§ and Norio Nemoto*,§

Department of Molecular and Material Sciences, IGSES, Kyushu University, Hakozaki, Fukuoka 812-8581, Japan, and Institute of Polymer Composite, Department of Polymer Science and Engineering, Zhejiang University, Hangzhou 310027, China

Received March 19, 2004; Revised Manuscript Received June 10, 2004

ABSTRACT: Simultaneous measurements of microscopic infrared (MicIR) dichroism, mesoscale deformation, and macroscopic stress during uniaxial stretching are made to four microphase-separated poly(ether-*block*-amide) (PEBA) films quenched form melt. Before the onset of microstructural alterations, poly(tetramethylene oxide) (PTMO) blocks in soft domains undergo affine deformation, and the true stress−strain relationship on the mesoscale of 500 μm can be described using an interpenetrating network model combining the Matsuoka viscoelastic constitutive equation and the affine deformation equation for mechanically hard and soft networks, respectively. Beyond a threshold strain at which PTMO blocks in the soft network are fully extended, plastic deformation occurs in the hard domain composed of polyamide-12 (PA), which is accompanied by depression of the true stress toward values lower than the prediction of the interpenetrating network model and also by deviation of the molecular orientation of PTMO blocks in the soft domain from the affine deformation mode. The deformation in the hard domain is characterized by a three-stage molecular orientation of hard PA blocks being present in either a fibrillar or a lamellar form. Alignment of PTMO blocks along the draw axis is predominantly observed for the sample with the lowest PA fraction, followed by rotation of the lamellae and then by the plastic deformation leading to fibrillation at high strains.

Introduction

Thermoplastic elastomers (TPEs) consisting of two chemically distinct segments are superior in their processing and recycling in comparison with conventional vulcanizates and thus received extensive interests from an industrial viewpoint. Because of the repulsive interaction or the thermodynamic incompatibility between the two constituent segments, microphase separation inevitably occurs and results in a heterogeneous structure of the hard and the soft domains, which is strongly responsible for the mechanical properties of the final products.[1] Hard domains are either glassy or crystalline at room temperature and act as physical cross-linking sites whereas soft segments are usually in the random-coil conformation and render the long-range elasticity.

Polarized Fourier transform infrared (FTIR) spectroscopy has been extensively used to study the molecular orientation and is particularly suitable for investigating multicomponent systems such as polymer blends, copolymers, and semicrystalline polymers because the molecular orientation of the different constituent components can be determined independently. It has been reported from infrared dichroism studies that segments in the two domains of TPEs behave quite differently during uniaxial deformation.[2−6] Soft segments are oriented toward the draw axis (orientation function $f > 0$) during uniaxial stretching up to break, while segments in hard domains usually shows a two-stage orientation, i.e., a perpendicular orientation ($f < 0$) at small strains followed by a parallel orientation ($f > 0$) at large strains. Desper et al.[7] studied microstructural deformation in polyurethanes by small-angle X-ray scattering (SAXS) as a function of macroscopic tensile strain and demonstrated three possible modes of shear, tensile, and rotation for the lamellar domains depending on the initial domain orientation with respect to the draw axis. At low strains, soft segments between two adjacent hard domains with their long domain axes perpendicular to the draw axis are extended along the draw axis via the lamellar separation or the tensile mode, causing an increase in lamellar long spacing. The deformation mode of hard domains with their long domain axes parallel to the draw axis is dominated by lamellar slip or shear compression accompanied by a decreased long spacing in the meridional direction. The exact contribution of each deformation mode depends on the inclination angle of a lamellar domain with respect to the draw axis. Despite the above-mentioned remarkable achievements, there still remains an issue how the stress−strain behavior observed by uniaxial stretching is related to the respective segmental orientations in microphase-separated copolymers. To reveal the underlying deformation mechanism, it seems necessary to demonstrate respective contributions of the hard and the soft segments to overall deformation, taking their interactions on the molecular level into consideration.

Poly(ether-*block*-amide) (PEBA) containing polyamide-12 (PA) as a hard block and poly(tetramethylene oxide) (PTMO) as a soft block has been widely studied as a TPE.[8−15] PEBA block copolymers are of special interest due to their excellent mechanical strength and elastic properties over a wide temperature range. By varying the amounts and the block lengths of the hard and the soft segments, materials with a wide range of distinct mechanical properties can be covered. In this

† Part VI of Deformation Mechanisms of Polymer Thin Films by Simultaneous Kinetic Measurement of Microscopic Infrared Dichroism and Macroscopic Stress.

‡ Zhejiang University.
§ Kyushu University.
* To whom correspondence should be addressed. E-mail: nemo@mm.kyushu-u.ac.jp.

10.1021/ma0400620 CCC: $27.50
Published on Web 07/17/2004

Table 1. Characterization of PEBA Samples

sample code	3533	4033	5533	6333
M_{PA}	674	800	2925	3800
M_{PTMO}	1870	1060[19]	1780	1200
w_{PA}	0.271[18]	0.430[19]	0.622[18]	0.758[18]
n_H	3.42[18]	4.06	14.85[18]	19.30[18]
n_s	26.00[18]	14.72	24.70[18]	16.60[18]
n_S/n_H [a]	7.60	3.62	1.66	0.86
n_S/n_H [b]	7.36	3.63	1.66	0.87
N_b [c]	19.6	26.9	10.6	10
n	48	22	28	24
N_k	38	7.5	8.0	6.2
T_m(PTMO)/°C	6	2	5	ND[d]
T_g(PTMO)/°C	−77	−78	−70	ND
T_m(PA12)/°C	143	163	162	174
T_g(PA12)/°C	52	49	47	ND
X_c in PA	0.18	0.23	0.20	0.20

[a] From M_{PTMO} and M_{PA}. [b] From IR. [c] Average block numbers for the soft and the hard segments. [d] ND: not detected.

paper, four PEBA samples with different hard segment contents are selected as model polymers for revealing the deformation and the segmental orientation behaviors of block copolymers on the mesoscale of 500 μm. From simultaneous measurements of the macroscopic force exerted by the film and the microscopic infrared (MicIR) dichroism subjected to uniaxial stretching along with direct measurement of the local deformation in the close vicinity of a predetermined sampling area using internal marks with the photogrammetry, we are allowed to establish the dependencies of true stress and molecular orientations on the actual local deformation. Special attention will be paid to the interpretation of the respective orientations of the soft and the hard segments and their cooperation in determination of the true stress−strain relationship. The investigation is carried out using the method earlier established during uniaxial stretching of a film,[16] which has been proved quite effective to collect information on the mesoscale deformation and the molecular orientation in the isotactic polypropylene (iPP) films.

Experimental Section

Materials. The four PEBA copolymers, under the trademarks of 3533, 4033, 5533, and 6333, from Elf Atochem Inc. (France), were used as received in this study. The commercial PEBA pellets were melted and compression-molded at 210 °C for 5 min to make thin films, which were then quenched to room temperature. The final products are apparently homogeneous in morphology without any spherulites distinguishable under a polarized optical microscope.

The segmented PEBA multiblock copolymers have an average molecular weight of ∼50 000 g mol^{-1}.[17] From elemental analysis of PEBA 3533, 5533, and 6333 samples, Rezac and John[18] calculated the repeat unit numbers of PTMO and PA12, represented as n_S and n_H, respectively, in this study, and the weight fraction of the hard segment, w_{PA}, from which we evaluated the weight-average molecular weights, M_{PA} and M_{PTMO}, of the soft and the hard segments as shown in Table 1. In addition, we estimated the chemical composition for PEBA 4033 on the basis of the reference data of $M_{PTMO} = 1060$ and $w_{PA} = 43$.[19]

The n_S/n_H values can be also evaluated from the structural absorbances, A_S and A_H, of two bands belonging to the soft and the hard segments, respectively

$$\frac{A_S}{A_H} = \frac{\epsilon_S}{\epsilon_H}\frac{n_S}{n_H} \tag{1}$$

where ϵ_S and ϵ_H are the respective molar absorptivities. Equation 1 can be modified as

$$\frac{A_S}{A_H} = \frac{197\epsilon_S}{72\epsilon_H}\left(\frac{1}{w_{PA}} - 1\right) \tag{2}$$

taking into account the molecular weights 72 and 197 for the repeat units of the soft and the hard segments, respectively. We found that eq 2 could approximately describe the relationship between A(1369 cm^{-1})/A(3300 cm^{-1}) and w_{PA}, and a least-squares fitting yielded $\epsilon_S/\epsilon_H = 0.25$ with a correlation coefficient of 0.994. n_S/n_H was then estimated from eq 1 as listed in Table 1. Excellent agreement was achieved for n_S/n_H values from IR absorbance and from the segment molecular weight.

We also characterized the samples with differential scanning calorimetry (DSC) measurements using a DSC-8240B calorimeter with a TAS-100 controller (Rigaku). The measurements were performed from −100 to 200 °C with a heating rate of 2.0 K min^{-1} under a dry nitrogen atmosphere. The first run data were used for data analysis, and the second run gave almost the same result for 4033. The melting points, T_m(PTMO) and T_m(PA), and the glass transition temperatures, T_g(PTMO) and T_g(PA), for the soft and the hard phases, respectively, were determined from the DCS curves according to the standard procedures. The heat of melting was estimated from the endothermic peak of PA12, and the crystallinity in the hard phase, X_c(PA), was calculated using the enthalpy of fusion 246 J g^{-1} for pure polyamide-12.[20] Crystallinity in the soft phase was not determined since this phase already melted at room temperature where the IR measurement was done.

Apparatus. The equipment permits simultaneous kinetic measurement of macroscopic nominal stress σ_n and MicIR dichroism from a small sampling area during uniaxial stretching of a thin film at a constant elongation rate. The setup details of the equipment are described elsewhere.[16,21,22] The sample cell of the elongation device was mounted in the same compartment of FTIR system. The film was fastened between the two clamps that moved synchronously to the two opposite directions from the film center. A strain-gauge type of force transducer was used to measure the force exerted by the film during elongation, from which the nominal stress σ_n was evaluated using the cross section measured before deformation. The infrared beam was irradiated vertically on the film from the bottom, and the MicIR dichroic functions of selected bands were estimated from measurements of $AC(t) = A_{\parallel}(t) - A_{\perp}(t)$ and $DC(t) = A_{\parallel}(t) + A_{\perp}(t)$ sampled alternately at a time internal of 30 s. Here $A_{\parallel}(t)$ and $A_{\perp}(t)$ are the polarized spectra at stretching time t with the IR radiation parallel and perpendicular to the draw axis, respectively.

Method. The film was cut to rectangular-shaped specimens with a size of 10 × 3 mm^2 (length × width), fastened between the two clamps spanning a length of 2 mm, and stretched with a constant elongation rate $\dot{\epsilon}$ of 0.05 min^{-1} corresponding to a stretching speed of 0.1 mm min^{-1}. The viewing field for sampling of the MicIR dichroism signal was 500 × 500 μm^2. The resolution of the spectrometer and the scan coaddition number were 4 cm^{-1} and 10, respectively, as described in an earlier paper.[21]

All the measurements were performed at 30.0 ± 0.1 °C. It had been noticed experimentally that a substantial volume of material was sucked out of the gripped region into the working zone, which made evaluation of the macroscopic strain evaluated from variations in the gauge length meaningless for samples with a high PTMO content. On the other hand, necking-like localized deformation, being a characteristic of inhomogeneous deformation in semicrystalline polymer films,[16,22] might occur in samples with a high PA content. Therefore, it seems desirable to measure the precise strain in a predetermined small area directly with the photogrammetry in order to elucidate the molecular orientation mechanism of polymer films subjected to uniaxial stretching. Before stretching the films, a sampling area was predetermined as that exactly located in the film center where several hard objects in a size of several to ∼20 μm could be distinguished under the microscope, which may have been formed during quenching

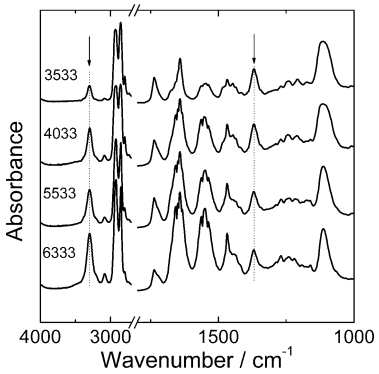

Figure 1. Spectra of PEBA films at 30 °C.

of the compression molded film. They might be the hard segment-rich domains and were thereby mechanically stable or less deformable in comparison with the submicron size of domains. One of the objects was pursued and adjusted to the viewing field under the microscope at a given time interval of 3 min moving the $x-y-z$ stage supporting the sample cell. A digital camera (Camedia C4040Z00M, Olympus Optical Co. Ltd.) connected with the ocular of the IR microscope was used to record micrographs of the sampling area just after the adjustment. The method of photogrammetry was employed for in-situ determination of the local strain within the sampling area to individual samples.[16] Distances between the objects in the sampling area were read from the micrographs in order to evaluate the mesoscale draw ratio λ_{Meso} in the length−width plane of the film. The true stress was derived from σ_n and λ_{Meso} as $\sigma = \sigma_n\lambda_{Meso}$, assuming incompressibility of the film during elongation. This assumption was proved to be the very good approximation for mesoscopic deformation of iPP films.[23]

From the dichroism of a desired absorbance band, the orientation function

$$f = \frac{3\langle\cos^2\theta\rangle - 1}{2} \tag{3}$$

can be derived from

$$f = \frac{2A(t)}{3 - A(t)}\frac{R_0 + 2}{R_0 - 1} \tag{4}$$

with

$$A(t) = \frac{AC(t)}{DC(t)} \tag{4a}$$

Here, θ is the orientation angle of a chain segment making with the draw axis, and $R_0 = 2\cot^2\psi$ is the perfect dichroic ratio of a transition moment, making an angle ψ with the direction of the molecular main-chain axis.

Results

Infrared Characterization of PEBA. The infrared spectra of PEBA films are shown in Figure 1. The possible assignments for the main infrared absorbance bands under interest are given in Table 2, together with their domain origins and orientation characteristics. A change in w_{PA} does not bring a marked variation in peak position of any vibration band. The weak and broad band complex composing three distinguishable peaks at around 1208, 1242, and 1260 cm^{-1} denote the various types of deformation taking place in the CH_2-O-CH_2 linkage of the soft segments. Another complex band ranged from 1405 to 1500 cm^{-1} are associated with the CH_2 units adjacent to NH and C═O groups in the extended chain conformation.[24] The peak centered at 1737 cm^{-1} is the symmetric stretching of the ester C═O group free of hydrogen bonding, which links the hard and the soft segments. The bands at 3145−3324 cm^{-1} (amide A), 1594−1694 cm^{-1} (amide I), and 1500−1590 cm^{-1} (amide II) are the characteristics of the amide groups belonging to the hard block.[25−27] In comparison with the absorption bands at 3445−3450 and 1700−1740 cm^{-1} of the N−H and C═O groups free of hydrogen bonding,[28] the observed positions of the amide A and the amide I vibrations shift to lower frequencies, indicating the hydrogen bonding association between the NH and the amide C═O groups in hard domains.

Table 2. Band Assignments for PEBA

band (cm^{-1})[a]	assignment[b,c]	ψ (deg)[b]	domain	orientation
1115(s)	ν_s(C−O−C)[3,25,29−31]	0	soft	∥
1208w)	t(CH_2)[32]		soft	∥
1242(w)	ν_s(C−O−C),[33] ω(CH_2)[32]		soft	∥
1260(w)	ν_{as}(C−O−C), amide III[33]		soft/hard	∥
1369(m)	ω(CH_2)[24,32]		soft	∥
1447(w)	δ(CH_2)[32]		hard	⊥
1467(w)	δ(CH_2),[33] γ(CH_2)[27]		hard	⊥
1565(m)	amide II[27]	0	hard	∥
1642(s)	amide I[26,29,31]	78	hard	⊥
1737(m)	ν(C═O) (ester)[28−30]	78	hard/soft	⊥
2796(m)	ν_s (CH_2)[32]		soft	⊥
2858(s)	ν_s(CH_2)[33]		hard/soft	/
2924(s)	ν_{as}(CH_2)[30,33]		hard/soft	/
3089(w)	amide B[34]		hard	⊥
3300(m)	amide A[27]		hard	⊥

[a] Terms in parentheses denote the band intensity (s: strong; m: medium; w: weak). [b] References in which the possible assignments can be found for polymers containing the same chemical units. [c] ν_s = symmetrical stretching, ν_{as} = asymmetrical stretching, δ = deformation, γ = bending, ω = wagging, t = twisting. Amide I = ν(C═O), amide II = δ(N−H) + ν(C−N), amide III = C−N−H vibration, amide A = ν(N−H), amide B = first overtone of amide II.

In this study, the isolated bands with medium intensities centered at 1369 cm^{-1} (the CH_2 wagging mode) and 3300 cm^{-1} (the amide A mode) were used to characterize the molecular orientations in the soft and the hard segments, taking $\psi = 0°$ and 90°, respectively. The bands of amide I and amide II show considerable dichroism, but they were not used for data analysis in this study because of the vibration complex dependent on the composition. It is to be noted that the amide A band gives the dichroism function consistent with that from the weak amide B band when w_{PA} is as high as in PEBA 6333. The broad band at 1115 cm^{-1} due to the C−O−C antisymmetric stretching mode is saturated when the PTMO content is high, which is therefore not suitable for deriving the molecular orientation of soft segments.

Time Profiles of σ_n, λ_{Meso}, and MicIR Dichroism. Figure 2 shows time profiles of macroscopic nominal stress σ_n as a function of stretching time t for the four PEBA films. The σ_n appears to increase as w_{PA} does. The films elastically deform at the earlier stage of elongation and yield at t = 10−17 min depending on the composition. The presence of a yield point in the stress−strain curve of a segmented copolymer indicates the existence of a continuous hard phase.[35,36]

Figure 3 shows time profiles of the orientation functions f_s and f_h for the soft and the hard segments, respectively. The soft segments are oriented toward the draw axis as found in TPE block copolymers, while the orientation of hard segments is considerably complicated and is different from the earlier findings in such a way that for the films of 3533, 4033, and 5533 their orienta-

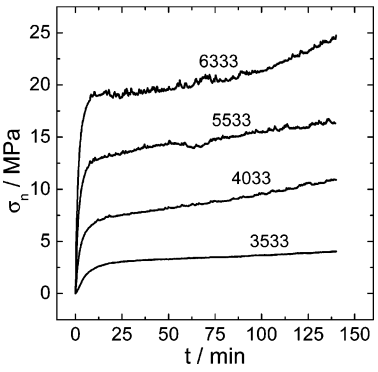

Figure 2. Nominal stress σ_n as a function of stretching time t for PEBA films drawn at 30 °C.

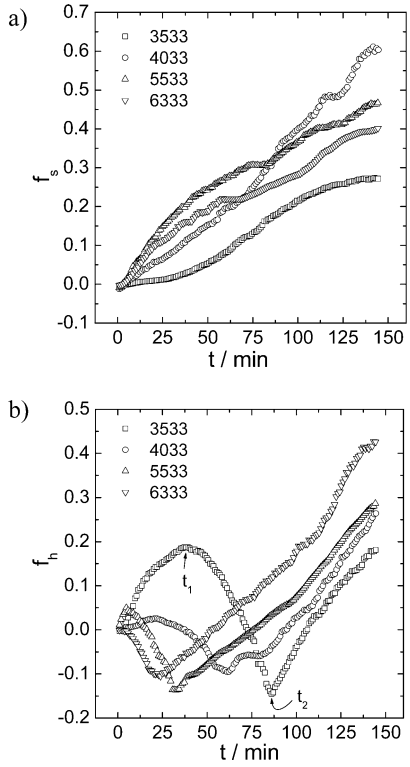

Figure 3. Orientation functions f_s and f_h of the soft (a) and the hard (b) domains as a function of stretching time t for PEBA films.

tion behaviors may be divided into three distinct time regions. The f_h increases with increasing strain in the first and the third regions whereas it decreases in the second one. The times t_1 and t_2, where the transitions from the first to the second and from the second to the third regions occur, are reduced with increasing w_{PA}. In the film of PEBA 6333, t_1 is not observed, and the hard segment only shows the two-stage orientation. The f_h values at t_1 for PEBA 4033 and 5533 are considerably lower compared with that for PEBA 3533. On the other hand, the f_h values at t_2 remain in a narrow region from −0.10 to −0.15, seemingly not much dependent on w_{PA}.

Discussion

Mesocale Deformation. Figure 4 shows the mesoscale draw ratio λ_{Meso} estimated with the method of photogrammetry. The measured value of λ_{Meso} as a function of time was fitted to a polynomial function $\lambda_{Meso} = 1 + \sum_j a_j t^j$, as shown by the solid curves in Figure 4. Here a_j is a coefficient associated with the jth power of

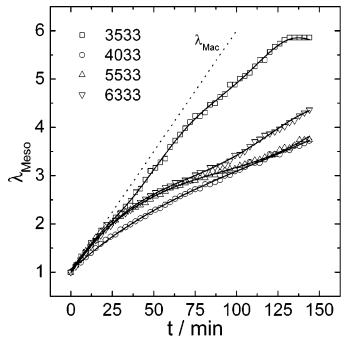

Figure 4. Mesoscale draw ratio λ_{Meso} in the predetermined sampling area plotted against stretching time t for PEBA films drawn at 30 °C.

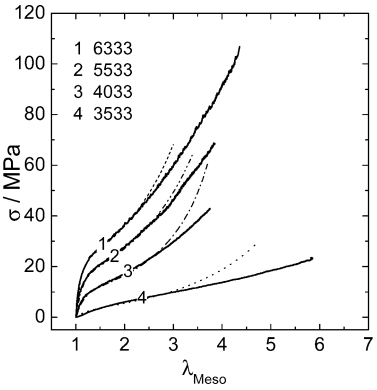

Figure 5. Plot of true stress σ against mesoscale draw ratio λ_{Meso} for the PEBA films. The solid curves are the experimental data and the dotted curves are calculated on the basis of eqs 5, 6, and 8.

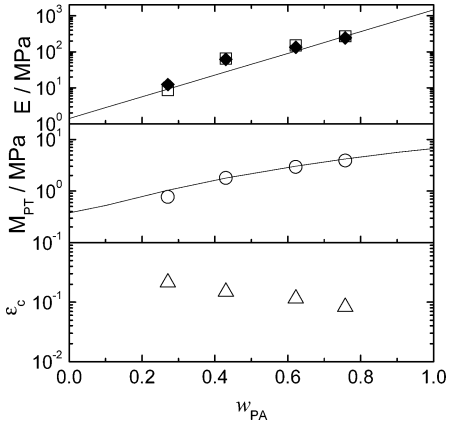

Figure 6. Plots of parameters describing the mesoscale deformation of PEBA films against hard segment content w_{PA}. The hollow symbols represent the fitted values, and the filled one is the Young's modulus estimated from the initial slope of the $\sigma-\lambda_{Meso}$ curves.

t. The fitting was made using the trial-and-error method until the calculated curve became considerably close to the measured data. The fitted curves using j up to 8, 3, 3, and 5 for the films of PEBA 3533, 4033, 5533, and 6333, respectively, can well map the measured data with a standard deviation of 0.019−0.039. The fitted polynomial function is then used to obtain true stress σ that is plotted against λ_{Meso} in Figure 5. As is clear from this figure, σ sharply increases at small λ_{Meso} followed by a monotonic increase with further increasing λ_{Meso}. From initial slopes of $\sigma_n-\lambda_{Meso}$ curves, Young's modulus was determined as presented in Figure 6 as a function of w_{PA}.

The two-phase model is generally accepted in the literature for describing the morphology of block copolymers, where the crystalline or the glassy hard domains are dispersed in an amorphous continuum composed of the soft phase and the amorphous hard segment. However, this model could not explain all the morphologies varying from spherulites to dendrites and to a lamellar network observed in block copolymer samples which experienced different preparation conditions.[37] In samples quenched from melt, a network structure of the hard segment tends to be formed by incorporating lamellar crystallites without predominated orientation.[35,37,38] The formation of a uniform network structure is considered to result from the coagulation contacts of the block domains.[39] Nishikawa et al. investigated the grain boundary morphology of lamellar microdomains in block copolymers by means of transmission electron microscopy (TEM).[40] With the aid of computer simulation, they found that the microdomains with lamellar morphology taking only a two-dimensional continuity locally are topologically continuous in the three-dimensional space as a whole through the grain boundaries. The lamellar network is mainly composed of the hard domains interlinked by short segments, which penetrate through the amorphous matrix forming another network. Recent works of Sauer et al. applying atomic force microscopy (AFM) imaging seem to support the interpenetrating network morphology in the solvent-cast film of PEBA 3533.[19,41] Sheth et al. also argued the existence of the connected hard phase in PEBA material, and the connectivity should increase with increasing the hard segment content, which results in a systematic increase in Young's modulus,[42] as shown in Figure 6.

On the basis of these studies aforementioned, we consider coexistence of two interpenetrating networks in the PEBA films. The first one named the hard network is the interconnected hard phase formed through the crystalline lamellae and a small fraction of soft segment as interdomain links. The second one, namely the soft network, consists of mainly the soft segments and a small fraction of the amorphous hard segment in the glassy state. Here the latter possibly behaves as cross-links together with some isolated lamellar hard domains at room temperature. The cooperative deformations of the two networks may be considered to occur so as to give rise to the true stress−strain relationship. Physically, the hard network is thermoplastic and the soft network elastic due to their T_gs higher and lower than room temperature, respectively. The mechanical response of the whole system changes from a typically elastic deformation to a plastic one with increasing the contribution of the hard network.

The formulation of the true stress−strain relationship may be done making use of the same idea for constructing the interpenetrating network model proposed for explaining the mesoscale deformation of the quenched iPP film with slight modification.[23] The stress σ_h arising from the hard network is assumed to be described using the Matsuoka equation[43] solving a constitutive equation for the Maxwell model with the modulus E and the relaxation time τ_M at constant strain rate as

$$\sigma_h = E\epsilon_C\left\{1 - \exp\left(-\frac{\epsilon_{Meso}}{\epsilon_C}\right)\right\} \quad (5)$$

Here $\epsilon_{Meso} = \lambda_{Meso} - 1$ is local strain, and $\epsilon_C = \dot{\epsilon}\tau_M$ is a characteristic strain. The σ_h should depend on temperature as well as the strain rate.

As shown by chemical composition in Table 1, the length of the PTMO chain segment is not large enough and is generally reduced with increasing w_{PA}. For understanding the deformation of the soft network, the limit drawability of the soft chains should be taken into account. The true stress−strain behavior of the soft network is likely to follow the prediction of the affine deformation model of nonGaussian statistics[44]

$$\sigma_s = \frac{\lambda_{Meso} NkTn^{1/2}}{3}\{L^{-1}(\lambda_{Meso} n^{-1/2}) - \lambda_{Meso}{}^{-3/2} L^{-1}(\lambda_{Meso}{}^{-1/2} n^{-1/2})\} \quad (6)$$

where k is Boltzmann's constant and T is the absolute temperature. N is the number of the soft segments per unit volume that determines the apparent shear modulus $M_{PT} = NkT$ of the soft network. n is the number of random PTMO links between effective cross-links such as small PA hard domains and chain entanglements. $L(x) = \coth x - 1/x$ is the Langevin function, and $L^{-1}(x)$ refers to its inverse. When n is large enough or λ_{Meso} is close to unity, eq 6 reduces to the Gaussian form

$$\sigma_s = M_{PT}(\lambda_{Meso}{}^2 - \lambda_{Meso}{}^{-1}) \quad (7)$$

Since the two networks are simultaneously stretched, total stress can be expressed as a sum of contributions from the two networks as

$$\sigma = \sigma_h + \sigma_s \quad (8)$$

Employing eqs 5, 6, and 8 with E, ϵ_C, and M_{PT} and n as adjustable parameters, fitting was made to the true stress−strain data, and the results are shown as the dotted curves in Figure 5. These fitted curves with values of n given in Table 1 and with the other three parameters as shown in Figure 6 well reproduce the measured data below $\lambda_{Meso} = 3.0$, 2.5, 2.6, and 2.8 for the films of PEBA 3533, 4033, 5533, and 6333, respectively. At high strains after the soft chains are fully extended, further extension likely causes the breakdown of hard domains in order to release stress. Downward deviations of the measured data from the model prediction at large strains reveal an irreversible microstructural alteration. We noticed that all the four samples showed tension set after unloading and the tension set increased with increasing w_{PA}.

If we would adopt the interpenetrating network model, the two networks must simultaneously respond to applied elongation spanning the whole sample volume and contributions from respective networks must depend on their fractions as well as their structures. The parameter E is almost the same as Young's modulus independently determined from the initial slope of the true stress−strain curves, revealing that the hard network supports the deformational stress at the earlier stage of stretching. M_{PT} in Figure 5 also increases with increasing w_{PA}. We found that E and M_{PT} can be related to w_P by the logarithmic additivity rule[45]

$$\log E = w_{PA} \log E_h + (1 - w_{PA}) \log E_s \quad (9)$$

and the Guth−Gold equation[46]

$$M_{PT} = G_s(1 + 2.5w_{PA} + 14.1w_{PA}{}^2) \quad (10)$$

In eqs 9 and 10, E_h is the elastic modulus of the PA

phase, and E_s and G_s are the elastic and the shear moduli of the soft phase, respectively. E_s and G_s values of the pure entangled PTMO network are estimated 1.4 and 0.38 MPa, respectively, from curve fitting of eqs 9 and 10 to the data in Figure 6, taking a reference value $E_h = 1.45$ GPa.[47] The value of E_s is a little bit larger than $3G_s$, but such a difference is not an unexpected result since the lowest w_{PA} value used for fitting was as high as 0.27.

Orientation of Soft Segments. To write eq 6, we assumed that the soft network deforms affinely, which should be further examined using the relationship between f_s and λ_{Meso}. The f_s in Figure 3a is replotted against λ_{Meso} in Figure 7a. It shows that the orientation of the soft segments at small λ_{Meso} can be described using the theoretical equation, eq 11, of the affine deformation of elastomers with limited segment extensibility,[48] consistent with the model used for prediction of the true stress−strain relationship in Figure 5.

$$f_s = \frac{1}{5N_k}\left(\lambda_{Meso}^{\,2} - \frac{1}{\lambda_{Meso}}\right) + \frac{1}{25N_k^{\,2}}\left(\lambda_{Meso}^{\,4} + \frac{\lambda_{Meso}}{3} - \frac{4}{3\lambda_{Meso}^{\,2}}\right) + \frac{1}{35N_k^{\,3}}\left(\lambda_{Meso}^{\,6} + \frac{3\lambda_{Meso}^{\,2}}{5} - \frac{8}{5\lambda_{Meso}^{\,3}}\right) + \Lambda \quad (11)$$

In eq 11, N_k is the average number of freely jointed Kuhn segments between cross-linking points. The fitted values of N_k are listed in Table 1. Same as the true stress−strain relationship, the soft segments are deformed affinely only if microstructural alterations are negligible. Above the λ_{Meso} value up to which the affine equation is applicable, f_s of 3533 deviates upward whereas f_s of 5533 and 6333 downward from the theoretical curves. In the film of 4033, eq 11 fairly describes the measured data in the whole range of deformation.

It is reported that the soft phase in PEBA materials will undergo strain-induced crystallization at ambient temperature.[48,49] We make an estimate of the induced crystallization from the absorbance of the CH_2 wagging mode at 1369 cm^{-1} using the symmetric stretching mode of the ester C═O group at 1737 cm^{-1} as a reference. The intensities of these two bands are comparable with each other for the four samples, and the absorbance ratio as a function of λ_{Meso} shows a decreasing tendency but is largely scattered, which could not provide a definite evidence for the induced crystallization of the soft segments taking place at high strains. For the sample 3533 containing the least PA amount, fibrillation of the whole soft chains might be the main process which gives rise to upward deviation of f_s from the prediction of eq 11. In samples of 5533 and 6333, destruction of large hard domains into small blocks may facilitate relaxation of oriented soft segments, which causes a downward deviation. Here, the molecular orientation of hard domains f_h should increase with λ_{Meso}, being in fair agreement with experimental data in Figure 7b. As given in Table 1, the average block number N_b is as large as 26.9 for the sample 4033; thus, the chain may be depicted as a linear sequence of hard and soft segments. For such a chain structure, the orientation of strain-induced fibrillar PTMO crystallites

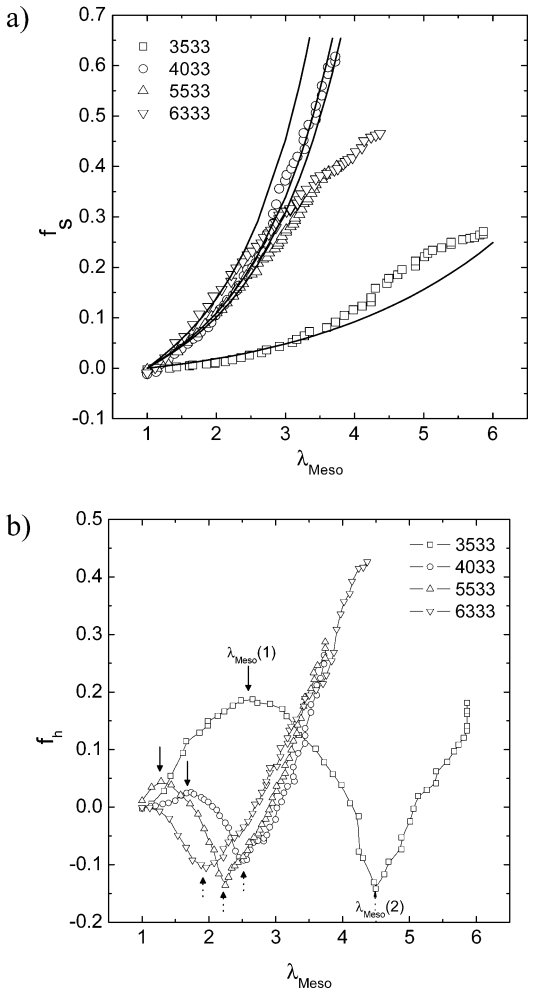

Figure 7. Orientation functions f_s and f_h for the soft (a) and the hard (b) domains as a funciton of mesoscale draw ratio λ_{Meso} for PEBA films.

may cancel out the relaxation of oriented soft segments due to destruction of hard domains and results in an apparent applicability of the affine deformation eq 11 for the f_s vs λ_{Meso} relation over the whole range of deformation tested.

Orientation of Hard Segments. In multiblock copolymers, hard segments may be present in either a fibrillar form composed of a small number of hard segments or a lamellar form,[51] and the latter fraction is expected to increase with an increase in the hard segment content. This classification is actually an oversimplified one, and there may exist broad distributions of the size and the aspect ratio for the hard domains formed through hydrogen bonding and crystallization during quenching of PEBA films from melt. Figure 8 illustrates how differently the two forms influence the microstructural deformations in PEBA films subjected to uniaxial stretching, which are unambiguously reflected in the λ_{Meso} dependence of f_h.

It is likely that the force exerted by the soft segments as well as the compression force causes the rotational orientation of both the lamellar and the fibrillar forms with their long axes toward to the draw direction. As is clear from Figure 8a, this rotational mode is observed as a decrease in f_h with increasing λ_{Meso} for the lamellar form with a large aspect ratio (R(L) mode) while as an increase in f_h for the fibrillar form with the main chain axis identical to the long axis (R(F) mode). We also must

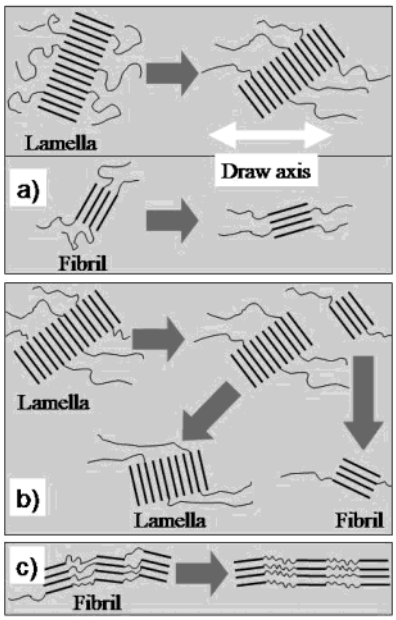

Figure 8. Illustration of various modes for microstructural deformation of the hard domains in PEBA films during uniaxial stretching. The thick short lines and the thin curves denote the hard and the soft segments, respectively. (a) Rotational modes R(L) and R(F), representing rotational orientaion of the lamellar and the fibrillar forms with their long axes toward to the draw direction, respectively. (b) Breakage mode B, denoting the breakdown of the long lamellar form into lamellar and fibrillar forms accompanied by their successive rotational modes, as well as instantaneous segmental orientation and relaxation in the soft phase during uniaxial stretching. (c) High orientation mode O(F), denoting fibrillation of PEBA chains by incorporating the parallel orientation of fibrillar forms and the strain-induced crystallization of soft segments.

consider that the lamellar form tends to break down into smaller sizes of lamellae and fibrils when highly strained (B mode), which may induce an increase in f_h and a relaxation of the soft segments with further drawing as shown in Figure 8b. On the other hand, it is assumed that the small and glassy fibril does not break and becomes more and more highly oriented at higher strains (O(F) mode), giving a sharp increase in f_h (Figure 8c). This may be regarded as definition of the "fibrillar form" used in this paragraph as the smallest size of the hard domain from the viewpoint of mechanical deformation. Here, the orientation behavior of soft segments follows the affine deformation in the rotation mode R(L) and R(F) modes, but may not in the B and O(F) modes.

While their contributions are strongly related to the level of stress as well as the PA content of respective films, the rotational orientations and the breakdown may happen simultaneously. The presence of a yield point in the nominal stress−strain curve (Figure 2) also suggests that the B mode may occur even at small strains, especially for lamellae with stack defects. However, modes R(L) and R(F) may be the main processes that dominate the microstructural deformation at $\lambda_{Meso} < \lambda_{Meso}(2)$ in Figure 7b because the measured f_s accords with the prediction from eq 11 approximately in the same strain range.

The complicated λ_{Meso} dependence of f_h observed for the film of PEBA 3533 shown in Figure 7b is interpreted as reflecting a consequence of successive occurrence of R(F), R(L), and then B plus O(F) modes. The fibrillar domains in the film can be easily oriented with small stress via the R(F) mode, which dominates over the perpendicular orientation of the coexisting lamellar domains via the R(L) mode and should be responsible for the initial parallel orientation. As the stress increases, remaining lamellar domains begin to rotate cooperatively to form a preferential alignment with their long axes parallel to the draw axis, which exceeds the chain axis orientation of fibrillar domains gradually and results in the second stage of perpendicular orientation in Figure 7b. Above $\lambda_{Meso} = \lambda_{Meso}(2)$, the plastic deformation of the hard domains via B mode accompanied by the O(F) mode becomes a dominative process that gives rise to a sharp increase in f_h.[4,52] This is consistent with an upward deviation of f_s from the prediction of affine model (Figure 7a). Furthermore, almost a linear increase in f_h for $\lambda_{Meso} > \lambda_{Meso}(2)$ implies fibrillation of the whole chain by incorporating the parallel orientation of hard segments and the strain-induced crystallization of soft segments.[41]

As the hard PA content increases, the fraction of the fibrillar form should decrease. Then an increasing trend of f_h with λ_{Meso} due to the R(F) mode may become less pronounced, and instead the R(L) mode appears at lower strain. Because of the decrease in the amount of soft segments, however, the sample cannot keep its original structure against applied stretching unless microstructural alteration due to B mode occurs at lower strain. These conjectures explain decreases in λ_{Meso} values at the minimum of f_h with increasing w_{PA} and overall λ_{Meso} dependence of f_h observed to the films of 4033 and 5533 for $\lambda_{Meso} < \lambda_{Meso}(2)$ in Figure 7b. For the PEBA 6333 film, the hard domains are mainly present as lamellar forms so that only a two-stage orientation of hard segments is observed.

The third stage of the parallel orientation process is closely related to B and/or O(F) modes. In taking into account that orientation behaviors of the soft segments in the films 5533 and 6333 are characterized by the downward deviation of f_s from the prediction of affine model at a strain close to the respective one at the f_h minimum, we may suppose that the B mode which allows chain relaxation of soft segments after consecutive destruction of hard lamellae into fibrils plays a prominent role for microstructural alteration in this strain region, and only a small portion of highly orientated chain might further undergo fibrillation. However, this supposition may not be applicable for the film 4033 with the block number as large as 27. The almost linear relation between f_h and λ_{Meso} with similar slopes observed for four PEBA films in the highly deformed region appears to wait for more elaborate theoretical analysis.

The structural transformation of the hard domains might be revealed using the absorbance ratio of the amide A band to a reference band insensitive to the deformation. Using the 1737 cm^{-1} band as a reference, the absorbance ratio $A_0(3300\ cm^{-1})/A_0(1737\ cm^{-1})$ was evaluated on the basis of

$$A_0(t) = \frac{DC(t)}{2} - \frac{AC(t)}{6} \tag{12}$$

and is plotted against λ_{Meso} in Figure 9 where the two characteristic local draw ratios $\lambda_{Meso}(1)$ and $\lambda_{Meso}(2)$ are also marked with arrows. $A_0(3300\ cm^{-1})/A_0(1737\ cm^{-1})$ increases very slightly or remains constant for $\lambda_{Meso} < \lambda_{Meso}(1)$, while it starts to decrease from a mesoscale draw ratio located between $\lambda_{Meso}(1)$ and $\lambda_{Meso}(2)$. The

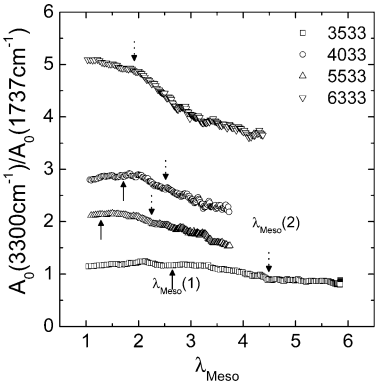

Figure 9. Absorbance ratio of the band 3300 cm^{-1} to the band 1737 cm^{-1} as a function of mesoscale draw raiton λ_{Meso}.

decrease in this absorbance ratio is considered to reflect partial breakdown of hydrogen bonding followed by the plastic deformation in the hard domains where the rotational orientation domain also occurs. The breakage of hydrogen bonding becomes more marked as increasing w_{PA}. For $\lambda_{Meso} > \lambda_{Meso}(2)$, the absorbance ratio remains approximately constant in the sample of 3533 whereas it continuously decreases in the other samples.

Conclusion

The deformation behavior of four quenched PEBA films is studied executing simultaneous measurements of MicIR dichroism, mesoscale strain, and macroscopic stress during unixial stretching at a constant elongation rate and at room temperature. The true stress−strain relationships on the mesoscale of 500 μm can be formulated using the interpenetrating network model up to medium strains, where the affine deformation of the soft network is validated in f_s as a function of λ_{Meso}. The three-stage orientation of hard segments is interpreted as being due to the competition of the chain axis orientation and the breakdown of hard domains with different sizes and aspect ratios. The rotation of hard domains mainly contributes to the first parallel and the second perpendicular orientations $\lambda_{Meso} < \lambda_{Meso}(2)$. The fibrillation of whole chains in the sample 3533 and the destruction of hard lamellae into fibrils in the other samples lead to the monotonic increase of f_h beyond $\lambda_{Meso}(2)$ dependent on the PA content.

Acknowledgment. This work has been partially supported by the Grant-in-Aid for the Scientific Research from Ministry of Education, Science, Sports and Culture, Japan (No. 10305070), and one of the authors, Y. Song, is grateful to JSPS for the Grant-in-Aid for JSPS Fellows relating to JSPS Fellowship for Foreign Researchers (No. 12000317).

References and Notes

(1) Holden, G. *Encycl. Polym. Sci. Eng.* **1986**, *5*, 416.
(2) Lee, H. S.; Lee, N. W.; Paik, K. H.; Ihm, D. W. *Macromolecules* **1994**, *27*, 4364.
(3) Wang, C. B.; Cooper, S. L. *Macromolecules* **1983**, *16*, 775.
(4) Reynolds, N.; Spiess, H. W. *Macromol. Chem. Phys.* **1994**, *195*, 2855.
(5) Estes, G. M.; Seymour, R. W.; Cooper, S. L. *Macromolecules* **1971**, *4*, 452.
(6) Lilaonitkul, A.; West, J. G.; Cooper, S. L. *J. Macromol. Sci., Phys. B* **1976**, *12*, 563.
(7) Desper, C. R.; Schneider, N. S.; Jasinski, J. P. *Macromolecules* **1985**, *18*, 2755.
(8) Deleens, G.; Foy, P.; Mare'chal, E. *Eur. Polym. J.* **1977**, *13*, 337.
(9) Mumcu, S.; Burzin, K.; Feldmann, R.; Feinauer, R. *Angew. Makromol. Chem.* **1978**, *74*, 49.
(10) Castaldo, L.; Maglio, G.; Palumbo, R. *J. Polym. Sci., Polym. Lett. Ed.* **1978**, *16*, 643.
(11) Gaymans, R. J.; Schwering, P.; de Haan, J. L. *Polymer* **1989**, *30*, 974.
(12) Van Hutten, P. F.; Walch, E.; Veeken, A. H. M.; Gaymans, R. J. *Polymer* **1990**, *31*, 524.
(13) Chung, L.-Z.; Kou, D.-L.; Hu, A. T.; Tsai, H.-B. *J. Polym. Sci., Part A: Polym. Chem.* **1992**, *30*, 951.
(14) Acevedo, M.; Fradet, A. *J. Polym. Sci., Part A: Polym. Chem.* **1993**, *31*, 1579.
(15) Yu, Y. C.; Jo, W. H. *J. Appl. Polym. Sci.* **1994**, *54*, 585.
(16) Song, Y.; Nitta, K.-H.; Nemoto, N. *Macromolecules* **2003**, *36*, 1955.
(17) Bondar, V. I.; Freeman, B. D.; Pinnau, I. *J. Polym. Sci., Part B: Polym. Phys.* **1999**, *37*, 2467.
(18) Rezac, M. E.; John, T. *Polymer* **1998**, *39*, 599.
(19) Sauer, B. B.; Mclean, R. S.; Brill, D. J.; Londono, D. J. *J. Polym. Sci., Part B: Polym. Phys.* **2002**, *40*, 1727.
(20) Xenopoulos, A.; Wunderlich, B. *J. Polym. Sci., Part B: Polym. Phys.* **1995**, *28*, 2271.
(21) Shigematsu, Y.; Takada, A.; Nemoto, N.; Nitta, K. *Rev. Sci. Instrum.* **2001**, *72*, 3927.
(22) Song, Y.; Shigematsu, Y.; Nitta, K.-H.; Nemoto, N. *Polym. J.* **2002**, *34*, 584.
(23) Song, Y.; Nitta, K.-H.; Nemoto, N. *Macromolecules* **2003**, *36*, 8066.
(24) Schoonover, J. R.; Thompson, D. G.; Osborn, J. C.; Orler, E. B.; Wrobleski, D. A.; Marsh, A. L.; Wang, H.; Palmer, R. A. *Polym. Degrad. Stab.* **2001**, *74*, 87.
(25) Ghosh, S.; Khastgir, D.; Bhowmick, A. K.; Mukunda, P. G. *Polym. Degrad. Stab.* **2000**, *67*, 427.
(26) Moriguchi, N.; Tsugaru, T.; Amiya, S. *J. Mol. Struct.* **1999**, *477*, 191.
(27) Rusu, G.; Ueda, K.; Rusu, E.; Rusu, M. *Polymer* **2001**, *42*, 5669.
(28) West, J. C. *J. Polym. Sci., Polym. Symp.* **1977**, *60*, 127.
(29) Kim, J. H.; Lee Y. M. *J. Membr. Sci.* **2001**, *193*, 209.
(30) Lee, H. S.; Ko, J. H.; Song, K. S.; Choi, K. H. *J. Polym. Sci., Part B: Polym. Phys.* **1997**, *35*, 1821.
(31) Ishihara, H.; Kimura, I.; Yoshihara, N. *J. Macromol. Sci., Phys. B* **1983**−**1984**, *22*, 713.
(32) Wang, Y.; Bazuin, C. G.; Pezolet, M. *Macromolecules* **2001**, *34*, 6344.
(33) Shen, D. *Application of Infrared Spectrum in Polymer Researches*; Science Press: Bejing, 1982.
(34) Cooper, S. J.; Coogan, M.; Everall, N.; Priestnall, I. *Polymer* **2001**, *42*, 10119.
(35) Cella, R. J. *J. Polym. Sci. Symp.* **1973**, *42*, 727.
(36) Grady, B. P.; Cooper, S. L. In *Science and Technology of Rubber*; Mark, J. E., Erman, B., Eirich, F. R., Eds.; Acadamic Press: San Diego, 1978.
(37) Zhu, L.; Wegner, G. *Makromol. Chem.* **1981**, *182*, 3625.
(38) Buck, W. H.; Cella, R. J.; Gladding, E. K.; Wolfe, J. R. *J. Polym. Sci. Symp.* **1974**, *48*, 47.
(39) Basirob, A. B.; Letunovskij, M. P.; Krjuckov, F. A.; Zelenev, Ju. V. *Acta Polym.* **1985**, *36*, 334.
(40) Nishikawa, Y.; Kawada, H.; Hasegawa, H.; Hashimoto, T. *Acta Polym.* **1993**, *44*, 247.
(41) Mclean, R. S.; Sauer, B. B. *J. Polym. Sci., Part B: Polym. Phys.* **1999**, *37*, 859.
(42) Sheth, J. P.; Xu, J.; Wilkes, G. L. *Polymer* **2003**, *44*, 743.
(43) Matsuoka, S. *Relaxation Phenomena in Polymers*, 2nd ed; Hanser: New York, 1992.
(44) James, H. M.; Guth, E. *J. Chem. Phys.* **1943**, *11*, 455.
(45) Wegner, G. In *Thermoplastic Elastomers*, 1st ed.; Legge, N. R., Holden, G., Schroeder, H. E., Eds.; Carl Hanser Verlag: Munich, 1987.
(46) Guth, E. *J. Appl. Phys.* **1945**, *16*, 20.
(47) Kohan, M. I., Ed. *Nylon Plastics Handbook*; Hanser Publishers: Munich, 1995.
(48) Roe, R. J.; Krigbaum, W. R. *J. Appl. Phys.* **1942**, *35*, 2215.
(49) Warner, S. *J. Elast. Plast.* **1990**, *22*, 166.
(50) Treloar, L. R. G. *Rep. Prog. Phys.* **1973**, *36*, 755.
(51) Bonart, R.; Muller-Riederer, G. *Colloid Polym. Sci.* **1981**, *259*, 926.
(52) Lee, H. S.; Yoo, S. R.; Seo, S. W. *J. Polym. Sci., Part B: Polym. Phys.* **1999**, *37*, 3233.

MA0400620